The Astrophysical Journal, 777:147 (8pp), 2013 November 10 doi:10.1088/0004-637X/777/2/147

NuSTAR DETECTION OF THE BLAZAR B2 1023+25 AT REDSHIFT 5.3

T. Sbarrato[1,2], G. Tagliaferri[2], G. Ghisellini[2], M. Perri[3,4], S. Puccetti[3,4], M. Baloković[5], M. Nardini[6], D. Stern[7], S. E. Boggs[8], W. N. Brandt[9,10], F. E. Christensen[11], P. Giommi[3,4], J. Greiner[12], C. J. Hailey[13], F. A. Harrison[5], T. Hovatta[5], G. M. Madejski[14], A. Rau[12], P. Schady[12], V. Sudilovsky[12], C. M. Urry[15], and W. W. Zhang[16]
[1] Dipartimento di Scienza e Alta Tecnologia, Università dell'Insubria, Via Valleggio 11, I-22100 Como, Italy; tullia.sbarrato@brera.inaf.it
[2] INAF-Osservatorio Astronomico di Brera, via E. Bianchi 46, I-23807 Merate, Italy
[3] ASI-Science Data Center, via Galileo Galilei, I-00044 Frascati, Italy
[4] INAF-Osservatorio Astronomico di Roma, via Frascati 33, I-00040 Monteporzio Catone, Italy
[5] Cahill Center for Astronomy and Astrophysics, California Institute of Technology, Pasadena, CA 91125, USA
[6] Dipartimento di Fisica G. Occhialini, Università di Milano Bicocca, Piazza della Scienza 3, I-20126 Milano, Italy
[7] Jet Propulsion Laboratory, California Institute of Technology, Pasadena, CA 91109, USA
[8] Space Sciences Laboratory, University of California, Berkeley, CA 94720, USA
[9] Department of Astronomy and Astrophysics, The Pennsylvania State University, 525 Davey Lab, University Park, PA 16802, USA
[10] Institute for Gravitation and the Cosmos, The Pennsylvania State University, University Park, PA 16802, USA
[11] DTU Space-National Space Institute, Technical University of Denmark, Elektrovej 327, DK-2800 Lyngby, Denmark
[12] Max-Planck-Institut für extraterrestrische Physik, Giessenbachstrasse 1, D-85748 Garching, Germany
[13] Columbia Astrophysics Laboratory, Columbia University, New York, NY 10027, USA
[14] Kavli Institute for Particle Astrophysics and Cosmology, SLAC National Accelerator Laboratory, Menlo Park, CA 94025, USA
[15] 1Department of Physics, Yale University, New Haven, CT 06520-8121, USA
[16] NASA Goddard Space Flight Center, Greenbelt, MD 20771, USA
Received 2013 August 12; accepted 2013 September 10; published 2013 October 23

ABSTRACT

B2 1023+25 is an extremely radio-loud quasar at $z = 5.3$ that was first identified as a likely high-redshift blazar candidate in the SDSS+FIRST quasar catalog. Here, we use the *Nuclear Spectroscopic Telescope Array* (*NuSTAR*) to investigate its non-thermal jet emission, whose high-energy component we detected in the hard X-ray energy band. The X-ray flux is $\sim 5.5 \times 10^{-14}$ erg cm^{-2} s^{-1} (5–10 keV) and the photon spectral index is $\Gamma_X \simeq 1.3$–1.6. Modeling the full spectral energy distribution, we find that the jet is oriented close to the line of sight, with a viewing angle of $\sim 3^\circ$, and has significant Doppler boosting, with a large bulk Lorentz factor ~ 13, which confirms the identification of B2 1023+25 as a blazar. B2 1023+25 is the first object at redshift larger than 5 detected by *NuSTAR*, demonstrating the ability of *NuSTAR* to investigate the early X-ray universe and to study extremely active supermassive black holes located at very high redshift.

Key words: galaxies: active – quasars: general – quasars: individual (B2 1023 + 25) – X-rays: general

Online-only material: color figures

1. INTRODUCTION

Blazars are radio-loud active galactic nuclei (AGNs) with a relativistic jet directed at a small angle from our line of sight (Urry & Padovani 1995). The peculiar orientation relativistically boosts the radiation emitted from their jets, making them visible even at high redshift (z).

The typical spectral energy distribution (SED) of a blazar is dominated by its non-thermal emission, characterized by two broad humps: the lower frequency component is attributed to synchrotron emission, while the higher frequency component is attributed to inverse Compton (IC) emission. The humps of a blazar SED peak at lower frequencies as the bolometric luminosity increases, at least for blazars studied to date (see, e.g., Fossati et al. 1998; Ghisellini et al. 2011 and Giommi et al. 2012 for different interpretations of the effect). At $z > 4$, we expect to see only the most powerful objects. Therefore, we should detect high-redshift sources whose synchrotron hump peaks in the sub-millimeter and whose IC hump peaks in the ∼MeV band. The synchrotron component shifts far enough out of the optical/UV to leave the accretion disk, usually swamped by non-thermal emission, visible (Sbarrato et al. 2013; Wu et al. 2013). The optical emission of a high-power, high-redshift blazar therefore becomes indistinguishable from that of a high-redshift, radio-quiet quasar. Since the accretion disk is visible, an estimate of the black hole (BH) mass can be obtained by fitting the emitted spectrum with a Shakura & Sunyaev (1973) accretion disk model (Calderone et al. 2013; Sbarrato et al. 2013).

The large redshift ($z > 4$) also moves the observed SED to lower frequencies. Therefore, the peak of the high-energy component appears well below 100 MeV (Ghisellini et al. 2010a, 2010b; Sbarrato et al. 2012). This introduces a challenge in identifying and classifying high-power, high-redshift blazars, since a classic hallmark of a blazar is detection by a γ-ray instrument like the Large Area Telescope (LAT) on the *Fermi* satellite (Atwood et al. 2009). Since the high-energy component peaks below 100 MeV, the identification of powerful high-redshift blazars in γ-rays is problematic.

On the other hand, sensitive hard X-ray telescopes can detect the high-energy hump of high-redshift, extremely powerful blazars. In fact, the Burst Alert Telescope (BAT) on board the *Swift* satellite (Gehrels et al. 2004) has detected blazars up to larger redshifts than the LAT (Ajello et al. 2009). The BAT blazars have hard X-ray spectra (i.e., $\alpha_X \lesssim 0.5$, assuming $F(\nu) \propto \nu^{-\alpha_x}$), and this, together with a strong X-ray to optical flux ratio, can be generally taken as a signature of the blazar nature of a source.

The most distant blazar known is Q0906+6930 (Romani et al. 2004; Romani 2006), located at $z = 5.47$. It was first classified as a blazar through a serendipitous EGRET 3σ detection. However, the more sensitive *Fermi*/LAT instrument did not detect the source, so the EGRET detection could either be

spurious or due to an episode of exceptional activity. Subsequent to its classification, Q0906+6930 was confirmed as a blazar through its X-ray and radio features (Romani 2006). In addition to being radio-loud, this source indeed shows a hard X-ray spectral index and high X-ray flux, leading to its classification as the most distant known blazar.

We identified the second most distant blazar known, B2 1023+25, at $z = 5.3$ (Sbarrato et al. 2012, hereafter S12). Its extremely large mass, $M_{\rm BH} = 2.8 \times 10^9\,M_{\odot}$, derived by fitting the accretion disk spectrum (see S12), makes this object particularly interesting, since it is possible to put relevant constraints on supermassive BH formation models using B2 1023+25 as a tracer of a population of very high-redshift, extremely massive BHs. Indeed, the observation of a single blazar with viewing angle $\theta_{\rm v}$ smaller than or comparable with the jet beaming angle (i.e., $\theta_{\rm v} < 1/\Gamma$, where Γ is the bulk Lorentz factor of the relativistic jet) indicates the possible presence of $2\Gamma^2$ analogous radio-loud, extremely massive AGNs with their jets directed in random directions. A typical blazar has $\Gamma \sim 15$, so finding even a few blazars at very high redshift is statistically very important for studying the population of extremely massive BHs. Therefore, this line of research could become competitive with searches for supermassive BHs at high redshifts using radio-quiet quasar samples: each blazar with $M_{\rm BH} > 10^9 M_{\odot}$ implies the presence of hundreds of analogous BHs in systems with a jet pointing elsewhere. Note that the usual radio-loud to radio-quiet ratio (10%) refers to objects with any BH mass. At the high-mass end, and at high redshift, this ratio could be larger (Volonteri et al. 2011; Ghisellini et al. 2013). The existence of $z > 5$ massive ($M_{\rm BH} > 10^9 M_{\odot}$) BHs in sources with powerful jets also raises challenges for BH growth models. Rapidly spinning (Kerr) BHs are often invoked as the energy source behind powerful jets (e.g., Wilson & Colbert 1995; Sikora et al. 2007). However, their accretion disks are radiatively very efficient ($L_{\rm d} = \eta \dot{M} c^2$, with $\eta > 0.1$, up to 0.3; Thorne 1974). As a consequence, over the same time interval, Eddington-limited Kerr BHs accrete *less matter* than Schwarzschild BHs. If this is the case, the time needed to form a $M_{\rm BH} \geqslant 10^9 M_{\odot}$ BH in a source with powerful jets is very long and no such systems should exist at $z > 4$ if they grow primarily through persistent accretion (Ghisellini et al. 2013).

B2 1023+25 was selected from a sample of $z > 4$ radio-loud sources as the best blazar candidate (Sbarrato et al. 2013; note that it was also listed as one of the most radio-loud quasars at $z > 4$ by Wu et al. 2013). We were able to observe the rising part of its high-energy hump due to a target of opportunity (ToO) observation with the X-Ray Telescope (XRT; Burrows et al. 2005) on board the *Swift* satellite (Gehrels et al. 2004). The hardness of the X-ray spectrum suggested that B2 1023+25 is a bona fide blazar. However, *Swift*/XRT observes at frequencies too low to properly sample the high-energy hump. This motivated our observation of B2 1023+25 with the *Nuclear Spectroscopic Telescope Array* (*NuSTAR*; Harrison et al. 2013). Indeed, a broader X-ray bandpass is required to properly classify B2 1023+25 by observing closer to the peak of the IC component. Due to its unparalleled broad-band sensitivity, *NuSTAR* is an ideal instrument to determine if the X-ray spectrum and flux of high-redshift candidates are hard and intense enough, respectively, to classify them as powerful blazars.

Here, we present *NuSTAR* observations of B2 1023+25 along with simultaneous observations obtained in multiple energy bands: X-ray observations from *Swift*/XRT, radio observations at three different frequencies from the Combined Array for Research in Millimeter-wave Astronomy (CARMA) and the Owens Valley Radio Observatory (OVRO), and seven-band optical- near-infrared (NIR) photometry from La Silla Observatory in Chile with the Gamma-Ray Burst Optical Near-Infrared Detector (GROND; Section 2). The X-ray data in particular allow us to constrain the high-energy component, thereby providing important insights into the orientation and Compton-boosting of B2 1023+25 (Section 3).

In this work, we adopt a flat cosmology with $H_0 = 70\,{\rm km\,s^{-1}\,Mpc^{-1}}$ and $\Omega_{\rm M} = 0.3$.

2. OBSERVATIONS AND DATA ANALYSIS

We performed simultaneous observations of B2 1023+25 with five instruments at different frequencies on UT 2013 January 1. The X-ray band was covered with *Swift*/XRT to check for possible variability with respect to our previous observations and *NuSTAR* to study the hard X-ray energy range. We added data from a previous *Chandra* observation (Wu et al. 2013) in order to increase the statistics of the soft X-ray energy band. We re-observed the source from La Silla (Chile) with GROND (Greiner et al. 2008), which provides simultaneous photometric data from the NIR to the optical in seven different bands. This re-observation was performed to check for possible variability of the thermal emission of the source. To have simultaneous radio data at three different frequencies, we observed B2 1023+25 with CARMA (Bock et al. 2006) and with the 40 m telescope at the OVRO. CARMA observed at 31 and 91 GHz (1 cm and 3 mm), while OVRO provided data at 15 GHz (2 cm). These data are combined with data from the *Wide-field Infrared Survey Explorer* (*WISE*[17]) satellite (Wright et al. 2010) and with archival data from NASA/IPAC Extragalactic Database and the ASI Science Data Center (ASDC[18]).

2.1. X-ray Observations

2.1.1. NuSTAR Observations

The *NuSTAR* satellite observed B2 1023+25 beginning on UT 2012 December 31 (sequence 60001107002) for a net exposure time of 59.3 ks. The two datasets obtained with the *NuSTAR* Focal Plane Modules A and B (FPMA and FPMB) were first processed with the NuSTARDAS software package (v.1.2.0), jointly developed by the ASDC and the California Institute of Technology (Caltech). Event files were calibrated and cleaned with standard filtering criteria with the `nupipeline` task using version 20130509 of the *NuSTAR* Calibration Database (CALDB).

The FPMA and FPMB spectra were extracted from the cleaned event files using a circular aperture with a 12 pixel ($\sim 30''$) radius, while the background was extracted from two distinct nearby circular regions with 30 pixel radii. The ancillary response files were generated with the `numkarf` task, applying corrections for the point spread function (PSF) losses, exposure maps, and vignetting. The source was detected up to 20 keV and the source spectrum in the 4–20 keV energy band was formed from a total of 79 counts (of which $\sim$44 are from the background) for FPMA and 113 counts (of which $\sim$58 are from the background) for FPMB. Both spectra were binned to ensure a minimum of 1 count per bin.

[17] Data retrieved from the *WISE* All-Sky Source Catalog: http://irsa.ipac.caltech.edu/.
[18] http://tools.asdc.asi.it/

2.1.2. Swift Observations

The *Swift* satellite observed the source three times: on UT 2012 June 21 (sequence 00032500001), on UT 2012 June 22 (sequence 00032500002), and on UT 2012 December 31 (sequence 00080499001). All XRT observations were carried out using the most sensitive photon counting readout mode.

The XRT dataset was first processed with the XRTDAS software package (v.2.8.0) developed at the ASDC and distributed by HEASARC within the HEASoft package (v. 6.13). Event files were calibrated and cleaned with standard filtering criteria with the `xrtpipeline` task using the latest calibration files available in the *Swift* CALDB.

The spectra obtained from the single observations are perfectly consistent, with an uncertainty on each measurement of ∼20%–25%, showing no variability among the three observations. We therefore merge the individual XRT event files, using the XSELECT package for a total net exposure time of 20.3 ks. Next, we extracted the average spectrum from the summed cleaned event file. Events for the spectral analysis were selected within a circular aperture with a 10 pixel (∼23″) radius, which encloses about 80% of the PSF, centered on the source position. The background was extracted from a nearby circular region with a 100 pixel radius. The ancillary response files were generated with the `xrtmkarf` task applying corrections for the PSF losses and CCD defects using the cumulative exposure map. The latest response matrices available in the *Swift* CALDB were used. The source spectrum in the 0.3–10 keV energy band was formed from a total of 41 counts (of which ∼3 are from the background) and it was binned to ensure a minimum of 1 count per bin.

2.1.3. Chandra Observations

B2 1023+25 was observed by *Chandra* on 2011 March for a total of ∼5 ks with the ACIS camera. These data were presented in Wu et al. (2013). In order to use them together with our other data sets, we re-extracted the *Chandra* spectrum. The data were reduced with the CIAO 4.4 package (Fruscione et al. 2006) using the *Chandra* CALDB version 4.4.7, adopting standard procedures. The source spectrum was extracted in a circular region centered on the peak of the X-ray source emission with a radius of 3″. The background spectrum was extracted from four circular regions with ∼5″radii, located around the source. The source spectrum in the 0.5–7 keV energy band was formed by a total of 54 counts (of which ∼1 is from the background) and it was binned to ensure a minimum of 1 count per bin.

2.1.4. X-ray Spectral Analysis

A comparison of the current and previous *Swift*/XRT observations discussed in S12 show that the source did not vary between these epochs. If we fit the data of each satellite alone, we find a good agreement among *NuSTAR*, XRT, and *Chandra*, but due to the faintness of the source the uncertainties are quite large. Since there is no evidence for variability, we performed a simultaneous fit of the *Swift*/XRT, *Chandra,* and *NuSTAR* spectra using the XSPEC package and adopting *C*-statistics (Cash 1979).

In prior work, the XRT and *Chandra* data were fit with a simple power-law model plus Galactic absorption (S12; Wu et al. 2013). In the present analysis, if we leave $N_{\rm H}$ free to vary, we find a high value for the absorption and a slightly steeper spectrum than previously reported. The statistical quality of the data is, however, not sufficient to distinguish between no absorption and spectral curvature and a higher level of intervening absorption and a steeper spectral index. X-ray absorption in the host of blazars is unlikely (the jet is able to completely ionize the host interstellar medium), but intervening material in high-redshift objects could be responsible for extra absorption. The presence or absence of extra absorption due to intervening material in quasar X-ray spectra is a matter of debate (see e.g., Vignali et al. 2005; Shemmer et al. 2005, 2006; Yuan et al. 2006; for a different point of view, see Behar et al. 2011), so we investigate fits with the column both fixed to the Galactic value and left free to vary. Both models provided a good description of the observed spectra (see Table 1). If we leave $N_{\rm H}$ free to vary, we find a high value of 2.8×10^{21} cm^{-2} assuming the absorbing material is at $z = 0$ (for higher redshift absorbers, this column increases). A simple power law plus Galactic absorption also provides an acceptable fit to the data: $\chi^2 = 230.5$ for 253 degrees of freedom (dof), to be compared with $\chi^2 = 211.3$ for 252 dof for the case where $N_{\rm H}$ is left free to vary. Although the χ^2 clearly improves when $N_{\rm H}$ is free to vary, the reduced χ^2 is already <1 with $N_{\rm H}$ fixed to the Galactic value; therefore, we cannot discriminate between the two possibilities from a statistical point of view. The results of the spectral fits are shown in Table 1. The photon spectral index in the two cases varies from $\Gamma_{\rm X} = 1.29^{+0.14}_{-0.15}$ to $\Gamma_{\rm X} = 1.60^{+0.27}_{-0.26}$. In the following analysis, we take this level of uncertainty in the spectral index into account, in particular in constraining the jet viewing angle (see Section 3). In Figure 1, we plot the X-ray SED of the source as derived with the spectral fit performed where $N_{\rm H}$ is left free to vary.

Table 1
Parameters of the X-Ray Spectral Analysis

$N_{\rm H}$ (cm^{-2})	$F_{\rm norm}$ (photons cm^{-2} s^{-1})	$\Gamma_{\rm X}$	$F_{5-10\,\rm kev}$ (erg cm^{-2} s^{-1})	χ^2/dof
1.5×10^{20} fixed	$1.29^{+0.29}_{-0.26} \times 10^{-5}$	$1.29^{+0.14}_{-0.15}$	5.8×10^{-14}	230.5/253
$2.8^{+2.0}_{-1.7} \times 10^{21}$	$2.26^{+1.16}_{-0.77} \times 10^{-5}$	$1.60^{+0.27}_{-0.26}$	5.5×10^{-14}	211.3/252

Note. The errors are at a 90% level of confidence for one parameter of interest.

2.2. GROND Observations

The 7-band GROND imager, mounted at the 2.2 m MPG/ESO telescope at La Silla Observatory, already stated previously started observing B2 1023+25 on UT 2013 January 1 at 07:38:43 UTC. We carried out three 8 minute observations simultaneously in all seven g', r', i', z', J, H, and K_s bands for a total exposure time of 1379 s in the optical and 1440 s in the NIR bands. Observations were carried out in an average seeing of 1.″2, evaluated from the r'-band image, and at an average airmass of 1.8. The source was clearly detected in all bands but g', for which an upper limit of 23.4 (AB magnitude) was found.

The GROND optical and NIR image reduction and photometry were performed using standard IRAF tasks (Tody 1993), similar to the procedure described in Krühler et al. (2008). A general model for the PSF of each image was constructed using bright field stars and it was then fit to the point source. The absolute calibration of the g', r', i', and z′ bands was obtained with respect to the magnitudes of Sloan Digital Sky Survey (SDSS) stars within the blazar field while the J, H, and K_s band calibration was obtained with respect to magnitudes of Two Micron All Sky Survey stars (Skrutskie et al. 2006).

Table 2 reports the observed AB magnitudes, not corrected for the Galactic extinction of $E(B - V) = 0.02$ from Schlegel

Table 2
GROND AB Observed Magnitudes of B2 1023+25, Obtained UT 2013 January 1

	g'	r'	i'	z'	J	H	K_s
$\lambda_{\rm eff}$ (Å)	4587	6220	7641	8999	12399	16468	21706
AB magnitude	>23.4	22.16 ± 0.16	19.91 ± 0.04	19.73 ± 0.03	19.52 ± 0.06	19.20 ± 0.09	19.35 ± 0.24

Notes. The first row lists the effective wavelengths of each filter (in angstroms). Magnitudes not corrected for Galactic extinction.

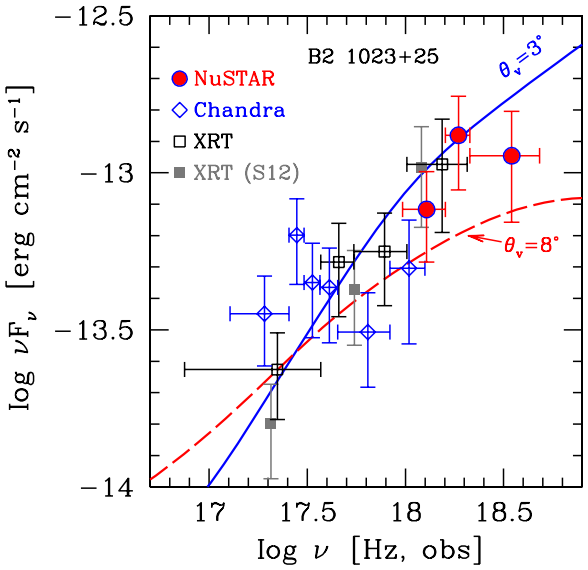

Figure 1. X-ray spectrum of B2 1023+25, along with the two SED models discussed in the text. *NuSTAR*/FPMB data are filled circles (red, circled in blue in the electronic version), *Chandra* data are empty diamonds (blue in the electronic version), and *Swift*/XRT data are open squares. The solid (blue) line is the model with $\theta_{\rm v} = 3°$, $\Gamma = 13$ and parameters as in the first row of Table 3. The dashed (red) line is the model with $\theta_{\rm v} = 8°$, $\Gamma = 10$ and parameters as in the second row of Table 3.

(A color version of this figure is available in the online journal.)

et al. (1998). Note that these data are fully consistent with those from S12, showing that the thermal emission of the source did not vary between the two observing times, as was also found for the X-ray non-thermal emission (see Section 2.1.4).

2.3. CARMA Observations

We observed B2 1023+25 at 31 and 91 GHz (1 cm and 3 mm, respectively) with CARMA. The observations were carried out simultaneously with the *NuSTAR* observation on UT 2013 January 1, with the array in the SL configuration. This configuration includes eight 3.5 m antennae on baselines of 5 to 85 m. Single sideband receivers were used to observe the upper and the lower sideband at 3 mm and 1 cm, respectively, and the correlator was configured to process 8 GHz of bandwidth. After flagging the bad data intervals, the total observation time was 3 hr in each band. Strong nearby sources 0956+252, 0927+390, and the planet Jupiter were used as gain, passband, and flux calibrators, respectively. The data were processed using the Multichannel Image Reconstruction Image Analysis and Display (Sault et al. 1995) software, optimized for CARMA. The observations reached an rms of 0.7 (1.5) mJy in the 1 cm (3 mm) band, providing a 47σ (9σ) detection of the target. The absolute flux density calibration, however, adds a systematic uncertainty of 10%, so the flux density values used in further analysis are $f_\nu(31\,{\rm GHz}) = 33 \pm 4$ mJy and $f_\nu(91\,{\rm GHz}) = 14 \pm 3$ mJy.

2.4. OVRO 40 m Observations

The OVRO 40 m telescope obtained a 15 GHz observation of B2 1023+25 simultaneous with *NuSTAR* on UT 2013 January 1. The telescope uses off-axis dual-beam optics and a cryogenic high electron mobility transistor low-noise amplifier with a 3 GHz bandwidth. The two sky beams are Dicke switched using the off-source beam as a reference and the source is alternated between the two beams in an ON–ON fashion to remove atmospheric and ground contamination. A noise level of approximately 3–4 mJy in quadrature with about 2% additional uncertainty mostly due to pointing errors is achieved in a 70 s integration cycle. The weighted average of nine consecutive integrations was used to derive the 15 GHz flux density $f_\nu(15\,{\rm GHz}) = 55 \pm 4$ mJy, where the systematic uncertainty in the absolute flux calibration has already been included. Calibration is routinely achieved using a temperature-stable diode noise source to remove receiver gain drifts and the flux density scale was derived from observations of 3C 286 assuming the Baars et al. (1977) value of 3.44 Jy at 15 GHz. Details of the reduction and calibration procedure can be found in Richards et al. (2011).

3. DISCUSSION

Figure 1 shows the X-ray data of B2 1023+25. The X-ray SED data points were all absorption corrected and rebinned to have a 3σ detection in each bin. Note that the *Swift*/XRT data are similar to those reported in S12 since variability is negligible. Given the rapid variability seen routinely in blazars at many wavelengths, this lack of variability is evidence that the electrons responsible for the hard X-ray emission have relatively small energies and thus lose energy slowly. This is consistent with X-rays produced through the so-called External Compton process (Sikora et al. 1994), in which relatively cold electrons scatter broadline photons. Also, the optical–UV emission is steady (see Section 2.2) for a completely different reason. This radiation is, in fact, emitted by the accretion disk, which is not expected to vary on short timescales.

The radio part of the spectrum shows flux variability both at 5 GHz and at high frequencies (see Figure 2). A 43 GHz flux density measurement was published recently by Frey et al. (2013), based on a Very Large Array A-configuration observation on UT 2002 June 19. A comparison of their $f_\nu(43\,{\rm GHz}) = 55 \pm 4$ mJy measurement with our CARMA measurements clearly shows that the radio flux is variable in time, as expected in blazars. The three radio data points obtained in this work define a spectral index $\alpha_{\rm r} \sim 0.7$ ($F(\nu) \propto \nu^{-\alpha_{\rm r}}$), steeper than the $\alpha_{\rm r} \sim 0.4$ value reported by Frey et al. (2013). At least in part, this could be due to the fact that the observed frequency of 91 GHz corresponds to ~570 GHz in the source rest frame, likely sampling the optically thin part of the synchrotron spectrum.

Due to the new X-ray flux results, we confirmed the extreme radio-loudness of B2 1023+25. During the sample

Table 3
Input Parameters Used to Model the SED

Γ (1)	θ_v (2)	R_{diss} (3)	R_{diss}/R_S (4)	P'_i (5)	B (6)	γ_b (7)	γ_{max} (8)	s_1 (9)	s_2 (10)	log P_r (11)	log P_B (12)	log P_e (13)	log P_p (14)
13	3	504	600	0.01	2.3	70	4e3	0	2.6	45.70	45.93	44.16	46.61
10	8	420	500	0.23	4.4	20	4e3	−1	2.6	46.72	46.11	45.72	48.26
5	20	588	700	7.0	5.5	2e3	4e3	−1	2.6	47.42	45.98	45.28	47.73

Notes. Column 1: bulk Lorentz factor, Column 2: viewing angle (degrees), Column 3: distance of the blob from the black hole in units of 10^{15} cm, Column 4: R_{diss} in units of the Schwarzschild radius, Column 5: power injected in the blob calculated in the comoving frame, in units of 10^{45} erg s^{-1}, Column 6: magnetic field in Gauss, Columns 7 and 8: minimum and maximum random Lorentz factors of the injected electrons, Columns 9 and 10: slopes of the injected electron distribution $[Q(\gamma)]$ below and above γ_b, Column 11: logarithm of the jet power in the form of radiation, Column 12: Poynting flux, Column 13: bulk motion of electrons, and Column 14: protons (assuming one cold proton per emitting electron). The spectral shape of the corona is assumed to be $\propto \nu^{-1}\exp(-h\nu/150\,\mathrm{keV})$. For all models, we have assumed a radius of the broadline region of $R_{BLR} = 9.2 \times 10^{17}$ cm, a BH mass of $2.8 \times 10^9\ M_\odot$, and an accretion disk luminosity of $L_d = 9 \times 10^{46}$ erg s^{-1}, corresponding to $L_d/L_{Edd} = 0.25$.

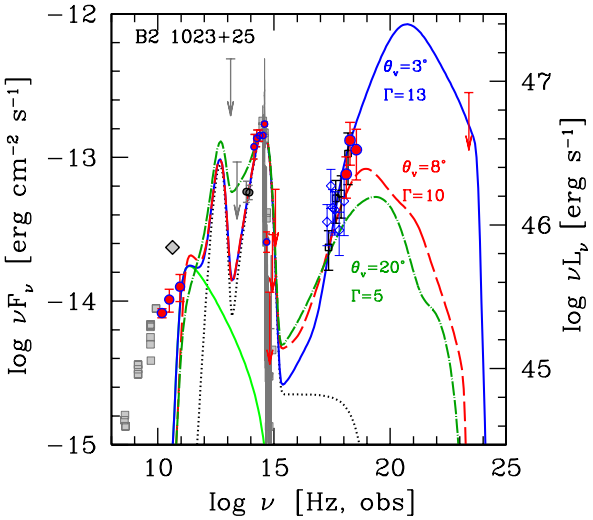

Figure 2. Broad-band SED of B2 1023+25 together with the models discussed in the text. Simultaneous OVRO, CARMA, GROND, and *NuSTAR* data are filled circles (red points circled in blue in the electronic version). *Chandra* data are open diamonds (blue in the electronic version), while *Swift*/XRT data are open squares. The (gray) filled symbols are data from the literature: squares are archival data from ASDC, the diamond is the radio point from Frey et al. (2013), the circles and the two upper limits are *WISE* data, and the line is the SDSS spectrum. The dotted (black) line is the thermal emission of the source, including the accretion disk, torus, and X-ray corona emission. The *Fermi*/LAT upper limit is for 3.8 yr, 5σ (red arrow). The solid (blue) line is the model with parameters as in the first row of Table 3. The dashed (red) line is the model with parameters as in the second row of Table 3. The dot-dashed (green) line is the model with parameters as in the third row of Table 3.

(A color version of this figure is available in the online journal.)

selection (Sbarrato et al. 2013), we used the canonical radio-to-optical ratio to define its radio-loudness ($R = F[5\,\mathrm{GHz}]/F[2500\,\text{Å}] \simeq 5200$) and this allowed to classify B2 1023+25 as the most radio-loud quasar of our sample. In addition to this, we now calculate the X-ray based radio-loudness $R_X = \nu L_\nu[5\,\mathrm{GHz}]/L_X[2\text{–}10\,\mathrm{keV}]$, using the X-ray fluxes and spectral indices listed in Table 1. We obtain $\log R_X = -0.65$ and $\log R_X = -0.72$ (for fixed and free N_H, respectively). Both values confirm the extreme radio-loudness of B2 1023+25 according to the calibration introduced by Terashima & Wilson (2003), which classifies quasars as radio-loud if they have $\log R_X > -4.5$.

In S12, we derived a set of parameters that reproduced the observed SED and suggested classifying B2 1023+25 as a blazar (bulk Lorentz factor $\Gamma = 14$; jet viewing angle $\theta_v = 3°$). We fit the new observations using the model described in Ghisellini & Tavecchio (2009). Since this is a one-zone model, which assumes that the emitting region is rather compact, it cannot account for radio emission, which in the considered region is severely self-absorbed.

In this model, both θ_v and Γ are free parameters and can be chosen independently.

Because of the hard and bright X-ray spectrum shown by B2 1023+25, we find a small value of θ_v and a large Doppler boosting (i.e., large Γ). We find $\theta_v < 1/\Gamma$, as is typical of known blazars. Hence, we confirm B2 1023+25 as a blazar (see Section 3.1).

Because of the limited statistics in the X-ray spectrum, we investigate the range of models consistent with the uncertainties. As noted above, depending on how the spectrum is modeled, the intrinsic continuum may be softer and fainter overall. This case implies a larger value of θ_v and a somewhat smaller value of Γ (see Section 3.2). The jet viewing angle, θ_v, associated with this limiting solution is an upper limit. Since this model is also characterized by less Doppler boosting, it corresponds to a larger intrinsic luminosity relative to the SED corresponding to the X-ray best fit parameters. We consider then "re-orienting" the jet to a typical blazar viewing angle (i.e., $\sim 3°$) and we check if the corresponding SED resembles the one of a typical powerful blazar seen at lower redshift. We then use this to check the reliability of the obtained solution; that is, we require that, if the jet was pointed toward us, the solution would show reasonably similar properties to the blazar sample.

In our modeling, we keep the parameters associated with the thermal emission from the accretion disk fixed. We assume a BH mass $M_{BH} = 2.8 \times 10^9 M_\odot$ and an accretion disk luminosity $L_d = 9 \times 10^{46}$ erg s^{-1}, as derived in S12. Note that varying the BH mass value inside the formal confidence range ($M_{BH} = 1.8\text{–}4.5 \times 10^9\ M_\odot$) does not change the results of our SED modeling.

3.1. Best Fit: Small Viewing Angle, Large Bulk Lorentz Factor

In our best fit model, we find a set of parameters consistent with those from S12 ($\Gamma = 13$, $\theta_v = 3°$). We report these in the first line of Table 3 as the best fit to the broad-band SED. The case in Table 3 corresponds to the best fit to the X-ray data with N_H left free to vary. Using N_H fixed to the Galactic value yields a harder spectrum and therefore an even more extreme blazar classification. The model (blue solid line in Figures 1, 2, and 3) describes a typical blazar, with a viewing angle smaller than the jet beaming angle ($\theta_v < 1/\Gamma$), firmly classifying B2 1023+25 as a blazar.

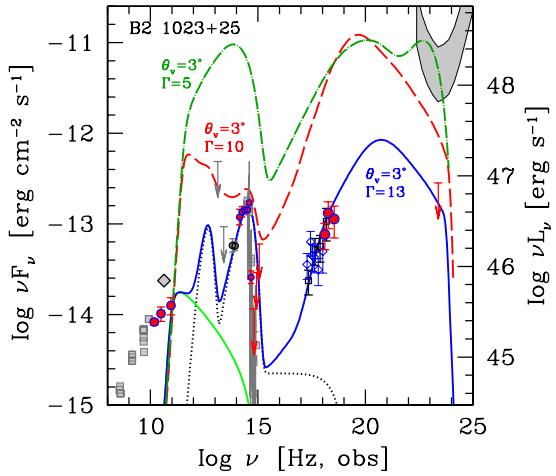

Figure 3. SED of B2 1023+25 with data as in Figure 2. The curved (gray) stripe corresponds to the sensitivity of *Fermi*/LAT after 1 yr of operation (5σ, lower bound) and 3 months (10σ, upper bounds). The solid (blue) line is the model with parameters as in the first row of Table 3. The dashed (red) line is the model with parameters as in the second row of Table 3 (i.e., $\theta_v = 8^\circ$), but "re-oriented" at $\theta_v = 3^\circ$, as labeled. The dot-dashed (green) line is the model with parameters as in the third line of Table 3 (i.e., $\theta_v = 20^\circ$), but "re-oriented" at $\theta_v = 3^\circ$, as labeled.

(A color version of this figure is available in the online journal.)

If $\theta_v < 1/\Gamma$, as in our best-fit model, the number of sources similar to B2 1023+25 but with the jet oriented outside of our line of sight is $2\Gamma^2 = 338(\Gamma/13)^2$ in the portion of the sky covered by SDSS+FIRST (Ghisellini et al. 2010a; Volonteri et al. 2011; Ghisellini et al. 2013). Since the combined SDSS and FIRST surveys (from which we selected B2 1023+25) cover together 8770 deg^2, this implies that in the whole sky there must be at least ∼1550 sources that share the same intrinsic properties of B2 1023+25. Since the co-moving volume in the redshift frame $5 < z < 6$ is ∼380 Gpc^3, we can conclude that there must be at least four radio-loud AGNs similar to B2 1023+25 per Gpc^3. Albeit extrapolating from a sample of one, this would imply the presence in the redshift bin $5 < z < 6$ of at least four supermassive BHs per Gpc^3, with a BH mass of $M_{\rm BH} \sim 10^9\ M_\odot$, hosted in jetted systems.

3.2. Slightly Misaligned Jet

Figure 1 shows that the X-ray data have large error bars. A softer X-ray spectrum cannot be excluded at a 90% confidence level (see Table 1). A softer spectrum implies a larger viewing angle and therefore a somewhat less extreme bulk Lorentz factor. Specifically, a viewing angle of $\theta_v = 8^\circ$ with $\Gamma = 10$, together with the other parameters in the second line of Table 3, still reproduce the broad-band data. The model (red dashed line in Figures 1 and 2) represents an alternative interpretation consistent with the X-ray data points at a 90% level of confidence. This viewing angle, slightly larger than the jet beaming angle $1/\Gamma$, still classifies B2 1023+25 as a blazar. As a consistency check, we test how an object with the same intrinsic (comoving) properties would look if oriented at $\theta_v = 3^\circ$, i.e., at $\theta_v < 1/\Gamma$. The re-oriented model is shown in Figure 3 by the dashed line (red dashed line in the electronic version). The resulting X-ray flux would be unusual but not unprecedented, being very similar, for example, to GB 1428+4217 ($z = 4.72$; Worsley et al. 2004), although the latter shows a synchrotron hump much dimmer than our "re-oriented" B2 1023+25. We conclude that $\theta_v = 8^\circ$ is the largest possible viewing angle consistent with the *NuSTAR* data.

If $\theta_v > 1/\Gamma$, as in the above case, the number of sources similar to B2 1023+25 but with their jet oriented in random directions is $1/(1 - \cos\theta_v)$. Hence, with $\theta_v = 8^\circ$, in the portion of sky covered by SDSS+FIRST, there would be 103 AGNs analogous to B2 1023+25 and in the whole sky there would be 469 (i.e., ∼1.2 object per Gpc^3). Even in this limiting case, the number of extremely massive BHs in jetted systems in the redshift bin $5 < z < 6$ is cosmologically significant.

3.3. Can the Jet be at 20° from our Line of Sight?

Frey et al. (2013) claim that a viewing angle of at least ∼20° with a bulk Lorentz factor $\Gamma \sim 15$ can be inferred for B2 1023+25 from published 5 GHz very long baseline interferometry (VLBI) imaging data. We therefore attempt to fit our X-ray data with $\theta_v = 20^\circ$ to test this hypothesis. We find that the data are not consistent with both a large viewing angle and a large Lorentz factor, i.e., the values obtained by Frey et al. (2013).

In this case, the corresponding Doppler factor $\delta = [\Gamma(1 - \beta\cos\theta_v)]^{-1} \sim 1$ and the intrinsic jet power become huge, to account for the observed X-ray flux (i.e., $P_{\rm jet} \sim 10^{50}$ erg s^{-1}). In addition, the fit to the observed data is poor.

The maximum bulk Lorentz factor providing a good fit to the *NuSTAR* and broad-band data with a viewing angle of $\theta_v = 20^\circ$ is $\Gamma = 5$ (along with the parameters in the third line of Table 3). This model is shown in Figure 2 as the dot-dashed line (green dot-dashed line in the electronic version). The corresponding beaming factor is $\delta \sim 2.5$. Such a modest beaming factor implies that the intrinsic luminosity would be very high. This would imply a class of objects with an extreme intrinsic luminosity. If such objects existed (at any redshift), we should see a few of them pointing at us. For illustration, we then "re-orient" B2 1023+25 to $\theta_v = 3^\circ$ (see Figure 3). Similar SEDs have never been observed, at any redshift. All powerful blazars observed so far have the Compton component dominating the overall SED, contrary to what is shown in Figure 3. We therefore believe that it is highly unlikely that B2 1023+25 can be described with $\theta_v = 20^\circ$ in the high-energy emitting region. We cannot exclude the possibility that the jet bends between the X-ray and the radio emitting regions. In this case, it is possible that the large-scale jet (i.e., the radio emission) is seen at a larger viewing angle than the compact jet.

Furthermore, consider that the 5 GHz VLBI observations analyzed by Frey et al. (2013) correspond to a rest-frame frequency of 31.5 GHz. At this frequency, all of the VLBI components except for the very inner core are emitting thin synchrotron radiation. Since the brightness temperature of a synchrotron source peaks at the self-absorption frequency, we conclude that all the brightness temperatures of the resolved components are lower limits. For the core, Frey et al. (2013) indeed performed a fit with a resolved plus an unresolved component. It is very likely that the resolved core is optically thin (thus giving a lower limit to the brightness temperature), while the unresolved core gives a lower limit because of the upper limit on the size. As a consequence, the derived Doppler factors are all lower limits and the derived viewing angles are all upper limits.

4. CONCLUSIONS

We selected B2 1023+25 as the best $z > 4$ blazar candidate from the SDSS+FIRST quasar catalog and we classified it as a blazar as the result of a *Swift*/XRT ToO observation (S12).

Here, we report simultaneous *NuSTAR* and *Swift* observations to improve the broad-band X-ray spectrum and further cement the blazar classification. We use the improved data to determine the jet orientation and the relativistic boosting factor. Simultaneous GROND data are important to check for possible variability. From the comparison with our first data, B2 1023+25 does not show variability in either its thermal or non-thermal emission.

We fit the broad-band SED with the model described in Ghisellini & Tavecchio (2009), focusing on the X-ray energy band as an important constraint, and we analyze in detail the non-thermal jet emission of the source. We confirm that B2 1023+25 is an extremely radio-loud quasar, with a jet oriented very close to our line of sight, and hence the Doppler boost is large. Our SED modeling indicates a small viewing angle ($\theta_v = 3^\circ$) associated with a large bulk Lorentz factor of $\Gamma = 13$. To account for the large X-ray data uncertainties, we tested solutions with larger viewing angles. A model with $\theta_v = 8^\circ$ and $\Gamma = 10$ cannot be excluded at the 90% uncertainty level by the data. A viewing angle larger than this is not consistent with the data and the resulting solution provides a lower limit to the real X-ray spectrum. Therefore, B2 1023+25 shows a jet orientation and a Doppler boosting that lead us to firmly classify it as the second most distant blazar known ($z = 5.3$). This implies the presence in the SDSS+ Faint Images of the Radio Sky at Twenty-centimeters (FIRST) survey of several detectable radio-loud sources with jets oriented in other directions. However, we have not been able to identify such objects in the survey; there are only four other radio-detected quasars in the SDSS+FIRST sample at $z > 5$. Although the statistics are small and possibly not constraining, the apparent inconsistency is addressed in Volonteri et al. (2011).

B2 1023+25 is the first object at $z > 5$ detected by *NuSTAR* and confirms that *NuSTAR* is a very useful instrument to deepen our knowledge of the high-redshift X-ray universe. Specifically, *NuSTAR* could be an ideal tool to continue the $z > 4$ blazar hunt. With the study of this single object, indeed, we were able to estimate, albeit with large uncertainty, how many extremely massive BHs in jetted sources are present at $5 < z < 6$. This constrains the mass function of heavy BHs in jetted systems as a function of redshift, which provides a complementary constraint for surveys of radio-quiet AGNs (see e.g., Ghisellini et al. 2013; Willott et al. 2010). The confirmation that B2 1023+25 is a blazar strengthens the suggestion of Ghisellini et al. (2013) that there are two epochs of heavy BH formation: radio-loud objects preferentially form their $M_{\rm BH} > 10^9 M_\odot$ BHs at $z \sim 4$, while radio-quiet quasars are formed at $z \sim 2$.

We thank the anonymous referee for useful comments. We acknowledge financial support from the ASI-INAF grant I/037/12/0. This work was supported under NASA Contract No. NNG08FD60C and made use of data from the *NuSTAR* mission, a project led by the California Institute of Technology, managed by the Jet Propulsion Laboratory, and funded by the National Aeronautics and Space Administration. We thank the *NuSTAR* Operations, Software, and Calibration teams for support with the execution and analysis of these observations. This research has made also use of the *NuSTAR* Data Analysis Software (NuSTARDAS) jointly developed by the ASI Science Data Center (ASDC, Italy) and the California Institute of Technology (Caltech, USA). The scientific results reported in this article are based in part on observations made by the *Chandra X-ray Observatory* and published previously in cited articles. This publication makes use of data products from the *Wide-field Infrared Survey Explorer*, which is a joint project of the University of California, Los Angeles, and the Jet Propulsion Laboratory/California Institute of Technology, funded by the National Aeronautics and Space Administration. Part of this work is based on archival data, software, or on-line services provided by the ASDC. This research has made use of the XRT Data Analysis Software (XRTDAS) developed under the responsibility of the ASDC, Italy. Part of the funding for GROND (both hardware as well as personnel) was generously granted from the Leibniz Prize to Professor G. Hasinger (DFG grant HA 1850/28-1). Support for CARMA construction was derived from the Gordon and Betty Moore Foundation, the Kenneth T. and Eileen L. Norris Foundation, the James S. McDonnell Foundation, the Associates of the California Institute of Technology, the University of Chicago, the states of California, Illinois, and Maryland, and the National Science Foundation. Ongoing CARMA development and operations are supported by the National Science Foundation under a cooperative agreement, and by the CARMA partner universities. The operation of the OVRO 40 m telescope is supported by NASA awards NNX08AW31G and NNX11AO43G and NSF awards AST-0808050 and AST-1109911. M.B. acknowledges support from an International Fulbright Science and Technology Award.

REFERENCES

Ajello, M., Costamante, L., Sambruna, R. M., et al. 2009, ApJ, 699, 603
Atwood, W. B., Abdo, A. A., Ackermann, M., et al. 2009, ApJ, 697, 1071
Baars, J. W. M., Genzel, R., Paulini-Toth, I. I. K., & Witzel, A. 1977, A&A, 61, 99
Behar, E., Dado, S., Dar, A., & Laor, A. 2011, ApJ, 734, 26
Bock, D. C.-J., Bolatto, A. D., Hawkins, D. W., et al. 2006, Proc. SPIE, 6267, 13
Burrows, D., Hill, J., Nousek, J., et al. 2005, SSRv, 120, 165
Calderone, G., Ghisellini, G., Colpi, M., & Dotti, M. 2013, MNRAS, 431, 210
Cash, W. 1979, ApJ, 228, 939
Fossati, G., Maraschi, L., Celotti, A., Comastri, A., & Ghisellini, G. 1998, MNRAS, 299, 433
Frey, S., Fogasy, J. O., Paragi, Z., & Gurvitis, L. I. 2013, MNRAS, 431, 1314
Fruscione, A., McDowell, J. C., Allen, GE., et al. 2006, Proc. SPIE, 6270, 62701V
Gehrels, N., Chincarini, G., Giommi, P., et al. 2004, ApJ, 611, 1005
Ghisellini, G., Della Ceca, R., Volonteri, M., et al. 2010a, MNRAS, 405, 387
Ghisellini, G., Haardt, F., Della Ceca, R., Volonteri, M., & Sbarrato, T. 2013, MNRAS, 432, 2818
Ghisellini, G., & Tavecchio, F. 2009, MNRAS, 397, 985
Ghisellini, G., Tavecchio, F., Foschini, L., et al. 2010b, MNRAS, 402, 497
Ghisellini, G., Tagliaferri, G., Foschini, L., et al. 2011, MNRAS, 411, 901
Giommi, P., Padovani, P., Polenta, G., et al. 2012, MNRAS, 420, 2899
Greiner, J., Bornemann, W., Clemens, C., et al. 2008, PASP, 120, 405
Harrison, F. A., Craig, W. W., Christensen, F. E., et al. 2013, ApJ, 770, 103
Krühler, T., Küpcü, Y., Greiner, J., et al. 2008, ApJ, 685, 376
Richards, J. L., Max-Moerbeck, W., Pavlidou, V., et al. 2011, ApJS, 194, 29
Romani, R. W. 2006, AJ, 132, 1959
Romani, R. W., Sowards-Emmerd, D., Greenhill, L., & Michelson, P. 2004, ApJL, 610, L9
Sault, R. J., Teuben, P. J., & Wright, M. C. H. 1995, in ASP Conf. Ser. 77, Astronomical Data Analysis Software and Systems IV, ed. R. A. Shaw, H. E. Payne, & J. J. E. Hayes (San Francisco, CA: ASP), 433
Sbarrato, T., Ghisellini, G., Nardini, M., et al. 2012, MNRAS, 426, L91
Sbarrato, T., Ghisellini, G., Nardini, M., et al. 2013, MNRAS, 433, 2182
Schlegel, D.-J., Finkbeiner, D. P., & Davis, M. 1998, ApJ, 500, 525
Shakura, N. I., & Sunyaev, R. A. 1973, A&A, 24, 337
Shemmer, O., Brandt, W. N., Schneider, D. P., et al. 2006, ApJ, 644, 86
Shemmer, O., Brandt, W. N., Vignali, C., et al. 2005, ApJ, 630, 729
Sikora, M., Begelman, M. C., & Rees, M. J. 1994, ApJ, 421, 153
Sikora, M., Stawarz, L., & Lasota, J. P. 2007, ApJ, 658, 815
Skrutskie, M. F., Cutri, R. M., Stiening, R., et al. 2006, AJ, 131, 1163
Terashima, Y., & Wilson, A. S. 2003, ApJ, 583, 145
Thorne, K. S. 1974, ApJ, 191, 507

Tody, D. 1993, in ASP Conf. Ser. 52, Astronomical Data Analysis Software and Systems II, ed. R. J. Hanisch, R. J. V. Brissenden, & J. Barnes (San Francisco, CA: ASP), 173
Urry, C. M., & Padovani, P. 1995, PASP, 107, 803
Vignali, C., Brandt, W. N., Schneider, D. P., & Kaspi, S. 2005, AJ, 129, 2519
Volonteri, M., Haardt, F., Ghisellini, G., & Della Ceca, R. 2011, MNRAS, 416, 216
Willott, C. J., Albert, L., Arzoumanian, D., et al. 2010, AJ, 140, 546
Wilson, A. S., & Colbert, E. J. M. 1995, ApJ, 438, 62
Worsley, M. A., Fabian, A. C., Celotti, A., & Iwasawa, K. 2004, MNRAS, 350, L67
Wright, E. L., Eisenhardt, P. R. M., Mainzer, A. K., et al. 2010, AJ, 140, 1868
Wu, J., Brandt, W. N, Miller, B. P., et al. 2013, ApJ, 763, 109
Yuan, W., Fabian, A. C., Worsley, M. A., & McMahon, R. G. 2006, MNRAS, 368, 985